Modulating interfacial electronic coupling of copper-mediated NiFe layered double hydroxide nanoprisms via structural engineering for efficient OER in wireless photovoltaic-coupled and anion exchange membrane water electrolysis

Debabrata Chanda [a,b], Hyunguk Kwon [c], Mikiyas Mekete Meshesha [a,b], Jang Seok Gwon [a,b], Minkyu Ju [d], Kyeounghak Kim [e], Bee Lyong Yang [a,b,*]

[a] School of Advanced Materials Science and Engineering, Kumoh National Institute of Technology, 61 Daehak-ro, Gumi-si, Gyeongbuk 39177, Republic of Korea
[b] GHS Co. Ltd., 61 Daehak-ro, Gumi-si, Gyeongbuk 39177, Republic of Korea
[c] Department of Future Energy Convergence, Seoul National University of Science & Technology, Seoul 01811, Republic of Korea
[d] Hyundai Energy Solution Co., Ltd. 9F, Global R&D Center, 477 Bundangsuseo-ro, Bundang-gu, Seongnam-si, Gyeonggi-do, 13553, Republic of Korea
[e] Department of Chemical Engineering, Hanyang University, 222, Wangsimni-ro, Seongdong-gu, Seoul 04763, Republic of Korea

ARTICLE INFO

ABSTRACT

In this work, a facile method is used to fabricate Cu-mediated NiFe-LDH (CuNiFe-LDH) nanoprisms from conductive metal–organic frameworks (MOFs; NiFe MIL-88A). The initial MOF structure is stabilized by electronic coupling and Cu ion coordination. The CuNiFe-LDH nanoprisms exhibit excellent OER performance, with an overvoltage of 204 mV at a current density of 10 mA cm^{-2} and a low activation energy of 15.45 kJ mol^{-1}. Mechanistic investigations using density functional theory calculations demonstrate that the Cu sites in CuNiFe-LDH are highly efficient for OER and that CuNiFe-LDH has a lower theoretical overpotential than NiFe-LDH. A wireless photovoltaic-electrochemical cell, developed using a CuNiFe-LDH/Ni fiber paper (NFP) anode and NiFe$_2$O$_4$/NFPcathode, achieves a solar-to-hydrogen efficiency of 11.08%. Additionally, the excellent performance of anion exchange membrane water electrolyzer incorporating the CuNiFe-LDH catalyst, including a j of 974 mA cm^{-2} at 1.85 V, and 46.9 kWh of electricity consumed per 1 kg of hydrogen produced.

1. Introduction

The generation of green hydrogen by solar-powered water splitting is beneficial for reducing fossil fuel dependency [1–3]. The oxygen evolution reaction (OER) requires highly active catalysts (such as RuO$_2$ and IrO$_2$), which are not suitable for commercial electrolysis [4–7]. Therefore, the development of affordable, durable, and active OER catalysts is both a practical necessity and major scientific challenge [8–10].

Currently, transition metal oxides, hydroxides, chalcogenides, phosphides, nitrides, and carbides of are receiving attention for the synthesis of next-generation catalysts because of their high abundance and stability under alkaline conditions [11–18]. Furthermore, crystalline metal–organic frameworks (MOFs) are important candidates for OER catalysts because of their adjustable morphologies and high active surface areas [19,20]. MOF-based hollow micro-/nanoprisms enhance catalysis by shortening OH$^-$ transport paths, reducing ion transport resistance, and increasing mass transport at the electrode/electrolyte interface. Specifically, the incorporation of MOF-based ultrathin nanosheets into NiFe-layered double hydroxide (LDH) nanoprisms has been found to enhance OER performance owing to electronic coupling between the Ni and Fe components [21–28]. Layered double hydroxide (LDH) is actually described by the general formula $[M^{II}_{1-x}M^{III}_x(OH)_2]^{z+}A^{n-}_{z/n}\cdot yH_2O$, where M(II) is a divalent metal cation and M(III) is a trivalent metal cation. LDH is a versatile material with a layered structure and a wide range of applications. Its unique properties, tunable composition and interlayer space make LDH attractive for catalytic and energy storage applications. [29] Although advanced (oxy)hydroxide catalysts with three-dimensional structures, such as nanospheres,

---

nanoprisms, and nanocages, have shown high OER activity,[30–33] their fabrication processes are complex and have limited scalability.

Tuning the morphologies and electronic structures of electrocatalysts are important strategies for further enhancing catalytic activity [34–37] Additionally, the introduction of additional metal ions can efficiently increase the catalytic activity by regulating the surface morphology and flexible coordination ability. Recently, doping with first-row transition metals, particularly Cu, has been investigated for enhancing electrocatalytic activity [38,39]. The high electron conductivity and D-electron abundance of Cu promote OH^- adsorption and electron transport at active sites [40,41]. Cu-containing catalysts have shown improved OER kinetics, with doped $Cu(Co_{0.21}Ni_{0.25})_3Se_2$ and core–shell Cu@NiFe LDH nanosheets achieving overpotentials (η) of 272 and 199 mV, respectively, at a current density (j) of 10 mA cm^{-2} [42,43]. Su et al. reported efficient OER catalysts consisting of a bimetallic sulfide (Ni_3S_2/Co_3S_4) doped with metals (Fe, Cu, Zn, and Mo) [44]. Density functional theory (DFT) calculations indicate that Cu ($3d^{10}4 s^1$), which is high in D-electrons, can transfer electron density from Ni^{2+} to Co^{2+}, leading to changes in the electron structure of the valence band and reduced OER adsorption energies (E_{ads}) for species such as OH* and OOH* . Nonetheless, such nanostructured catalysts mostly require complex multistep synthesis processes, which greatly restricts their suitability for large-scale applications.

As a powerful tool for producing efficient catalysts, a strategy to achieve both Cu doping and flexible coordination was rationally designed. A unique self-template approach was used to fabricate spindle-assembled nanoprisms of Cu-doped NiFe-LDH nanocages derived from an MOF (MIL-88A). As an OER electrocatalyst, the CuNiFe-LDH nanoprisms showed a η of 204 mV at $j = 10$ mA cm^{-2}. Indeed, the use of water splitting with sunlight using photovoltaics coupled to electrochemical cells (PV-EC) is an efficient method for generating clean fuels such as H_2. [45,46] Despite the potential of PV-EC cells for hydrogen production, there are still some challenges that need to be addressed, such as improving the efficiency and stability and cost of the system. Furthermore, the development of a wireless photovoltaic (PV) coupled electrochemical (EC) device (PV-EC) device for green hydrogen and oxygen production that could be used in aerospace and artificial leaf applications could have numerous benefits. In this study, we developed a wireless PV-EC device with a solar-to-hydrogen (STH) efficiency of 11.08% by combining an amorphous silicon (a-Si:H)/a-Si:H/microcrystalline silicon (μc-Si:H) trijunction thin-film solar cell with a CuNiFe-LDH/Ni fiber paper (NFP) anode and $NiFe_2O_4$/NFP cathode. In addition, practical electrolyzer systems need to be developed to enable the large-scale production of green hydrogen. Anion exchange membrane water electrolyzers (AEMWEs) are gaining popularity because of their advantages over alkaline water electrolyzers and proton exchange membrane water electrolyzers (PEMWEs) [13,47–49]. AEMWEs employ solid thin anion exchange membranes and non-platinum group metal electrocatalysts to significantly reduce capital costs [48,50]. For AEMWE commercialization, a j of > 0.9 A cm^{-2} at 1.85 V is required to match the performance of PEMWEs. Our electrolysis cell with a CuNiFe-LDH/NFP anode and a $NiFe_2O_4$/ NFP cathode achieved a j of 10 mA cm^{-2} at 1.45 V in conventional two electrode electrolyzers and a j of 974 mA cm^{-2} at 1.85 V in an AEMWE. These results demonstrate the effectiveness of CuNiFe-LDH nanoprisms derived from MIL-88A in promoting OER activity. The incorporation of highly conductive Cu ions into the NiFe-LDH structure increased the conductivity of the catalyst and allowed more efficient electron transfer during the OER. Thus, MOF-based CuNiFe-LDH nanoprisms have great potential for OER applications and provide an important information for the development of efficient and cost-effective electrocatalysts.

2. Experimental

2.1. Materials

$Ni(NO_3)_3$·6 H_2O, $Cu(NO_3)_3$·3 H_2O, $Fe(NO_3)_3$·9 H_2O, dimethylformamide (DMF), fumaric acid, and KOH were purchased from Alfa Aesar (USA). Commercial IrO_2 (99.9%) and Pt/C (20 wt%) were purchased from Sigma–Aldrich (USA). Ni fiber paper (NFP), Sustainion™ X37–50 RT membrane, and Sustainion™ XC-1 binder were purchased from Dioxide Materials (USA). A Millipore laboratory system was used to supply deionized water.

2.2. Catalysts synthesis

2.2.1. Preparation of MIL-88A metal–organic frameworks (MOFs)

Typically, $Fe(NO_3)_3$·9 H_2O (320 mg) and fumaric acid (160 mg) were mixed in DMF (25 mL)/H_2O (5 mL) over 3 days to form a red-yellow solution. After transferring the obtained solution to a Teflon-lined stainless steel autoclave (50 mL), a hydrothermal reaction was carried out at 90 °C for 6 h. The precipitate was collected by centrifugation, washed three times with a water/ethanol (1:1) mixture, and then dried at 60 °C for 10 h.

2.2.2. Preparation of NiFe-LDH nanoprisms

Solution A was prepared by dispersing MIL-88A (14 mg) in DMF (20 mL). Solution B was prepared by dissolving urea (200 mg) and Ni $(NO_3)_3$·6 H_2O (150 mg) in water (20 mL). Solution C, which was prepared by mixing solutions A and B, was heated at 90 °C for 6 h in a completely sealed Teflon-lined stainless autoclave (50 mL). The obtained product was washed three times with a water/ethanol (1:1) mixture and then dried at 60 °C for 10 h.

2.2.3. Preparation of CuNiFe-LDH nanoprisms

First, fumaric acid (200 mg) and urea (400 mg) were dissolved in water (30 mL) by stirring at room temperature. $Ni(NO_3)_3$·6 H_2O (150 mg), $Cu(NO_3)_3$·3 H_2O (50–200 mg), and $Fe(NO_3)_3$·9 H_2O (320 mg) were added to DMF (10 mL). The solutions were mixed and then transferred into a Teflon-lined stainless autoclave (50 mL), and a hydrothermal reaction was performed at temperature at 90 °C for 6 h. The obtained product was collected by centrifugation, washed three times with distilled water followed by ethanol, and dried at 60 °C for 1 day.

2.3. Alkaline water electrolyzer setup and operation

2.3.1. Washing and pretreatment of Ni fiber paper electrode

Activated nickel fiber paper (NFP) electrode has been used as an anode and cathode gas diffusion electrode in electrochemical reactions. NFP pieces with sizes of 1×1 and 5×5 cm^2 were cut from a commercial NFP. The NFP pieces were immersed in hydrochloric acid (0.1 M) and ultrasonicated for 15 min, rinsed with deionized water and ethanol, and dried in an oven at 60 °C for 6 h.

2.3.2. Gas Diffusion Electrode (GDL) preparation

The electrode was manufactured using a catalyst coating method. To prepare the anode, the catalyst (20 mg) was mixed with water (1 mL), isopropyl alcohol (2 mL), and anion exchange binder (Sustainion® XC-1; 100 μL) via ultrasonication for 30 min. A similar method was used to produce a $NiFe_2O_4$-coated cathode [13]. The catalytic loadings of the anode and cathode were ~2.5 mg cm^{-2}. The homogeneous catalyst ink was coated on an NFP GDL using the spray coating method on a hot plate (60 °C). The active area of the electrode was 5×5 cm^2. For comparison, RuO_2-coated NFP (catalyst loading: ~1 mg cm^{-2}) and 20% Pt/C-coated NFP (catalyst loading: ~0.5 mg cm^{-2}) were used as the anode and cathode, respectively.

2.3.3. Conventional two-electrode system

Conventional water electrolyzer testing was performed using a two-electrode single-chamber setup. CuNiFe-LDH/NFP and NiFe$_2$O$_4$/NFP were used as the anode and cathode, respectively, and the electrolyzer was tested at 1.45–1.9 V.

2.3.4. Wireless solar-driven water electrolysis

Bifacial a-Si:H/a-Si:H/μc-Si:H trijunction monocrystalline solar cells were fabricated using a laser scribing machine. The Ag side of the solar cell was cleaned with solder flux. Cu tape welded to one end of the solar panel (front and back sides) was used for connections. The *I–V* characteristics of the solar cells were determined using a Keithley 4200 source measure unit under simulated AM 1.5 G light (Oriel Sol3A Solar Simulator) at 100 mW cm^{-2} with a scan rate of 5 mV s^{-1} in the direction from the open-circuit voltage to the short-circuit current. The light intensity was calibrated using a 91150 V Reference Cell and Meter (Newport). The bias voltage for steady-state measurements was chosen as the average maximum power point voltage during *I–V* measurements. The solar cells (Type A, B1, B2, B3, B4, B5, and combined) exhibited voltages of 0.35, 0.35, 0.35, 0.35, 0.35, 0.35, and 2.1 V, respectively. Two types of solar cell devices (flat and semicircular) were manufactured. Finally, the PV-EC system was sealed with steelweld epoxy (Hardex, Malaysia).

2.3.5. Commercial anion exchange membrane water electrolyzer (AEMWE)

A membrane electrode assembly (MEA) was prepared by placing membrane (Sustainion™ X37–50 RT) between two catalyst-coated substrates (catalyst coated NFP electrodes) using the hot press method (2 MPa, 40 °C, 1 min). For comparison, an MEA was also manufactured using the catalyst-coated membrane (CCM) method and catalyst coated substrate (CCS) method. In CCM method, the catalyst loading on the top of the membrane is approximately 1.0 mg cm^{-2}. The compositions of the prepared MEAs are listed in Table S1. Prior to MEA preparation, the membrane was activated by immersion in 1 M KOH for 24–48 h to convert the chloride form into the hydroxide form. Finally, the AEMWE cell was constructed using various components, including the MEA, a silicon gasket, and a flow field with a Ti current collector/endplate. Electrolyzer operation was evaluated using an applied potential of 1.4–2 V at operating temperature of 50 °C. Finally, two stainless steel endplates were used to compress the AEMWE with a torque of 3.32 N.m. The electrolyzer configuration and operational details are described in our previous study [51]. The performance of the AEMWE was evaluated based on *I–V* curves and EIS data, as measured using a DC power supply (GW-INSTEK SPS-1230, Taiwan) and apotentiostat (ZIVE SP1 potentiostat), respectively. The electrolyzer cell efficiency at lower heating value (LHV) was evaluated as:

$$\text{Cell efficiency} : \frac{\Delta H_2 \times \eta_{H2}}{I \times V} \times 100 \tag{1}$$

where ΔH_2 is the reaction enthalpy of water electrolysis (241.8 kJ mol^{-1}) at the LHV, η_{H2} is the rate of hydrogen production (mol s^{-1}), I is the applied current (A), and V is the applied voltage (V).

3. Results and discussion

3.1. Surface morphology and structural analysis

CuNiFe-LDH nanoprisms were synthesized as outlined in Scheme 1. First, a sacrificial template is fabricated using Fe(NO$_3$)$_3$·6 H$_2$O and fumaric acid to create an Fe-MOF (MIL-88A) with a uniform smooth surface. Second, NiFe-LDH and CuNiFe-LDH are prepared using Fe-MOF, urea, and Ni or Ni and Cu precursors, respectively. The ICP-OES (Inductively Coupled Plasma Optical Emission Spectrometry) was used to measure the Cu, Ni, and Fe concentrations in CuNiFe-LDH and the results were recorded in Table S2. Optimization of the Cu concentration in NiFe-LDH for OER activity revealed that 30% Cu doping provides the best performance (Fig. S1). Field-emission scanning electron microscopy (FESEM) reveals that Fe-MOF has a smooth spindle-like shape (Fig. 1a). Fe-MOF is subsequently converted into NiFe-LDH nanoprisms (Fig. 1b and S2) or CuNiFe-LDH nanoprisms (Figs. 1c and S3). Energy-dispersive X-ray spectroscopy (EDX) analysis confirms the presence of Cu, Ni, and Fe in the CuNiFe-LDH nanoprisms (Fig. S4). The diffraction peaks at 11.3°, 22.7°, and 34.5° in the XRD pattern of the CuNiFe-LDH nanoprisms (Fig. S5) correspond to the (003), (006), and (012) planes, respectively of CuNiFe-LDH (JCPDS No. 40–0215). Transmission electron microscopy (TEM) images (Fig. 1d) reveal interconnected Fe-MOF nanoprisms, and EDX elemental mapping confirms the presence of Fe (Fig. 1e,f). Similarly, TEM images (Fig. 1g) and EDX elemental mapping (Fig. 1h–j) of the NiFe-LDH nanoprisms show a uniform distribution of Ni and Fe. The TEM image of CuNiFe-LDH (Fig. 1k) reveal a loosely packed porous structure, confirming the successful synthesis of hierarchical nanoprisms. Furthermore, a high-resolution TEM (HRTEM) image (Fig. 1j) indicates the presence of two phases: 012 (0.26 nm) and 006 (0.347 nm) [39]. Finally, EDX elemental mapping of CuNiFe-LDH (Fig. 1m–p) confirms the uniform distribution of Cu, Ni, and Fe throughout the porous nanoprisms.
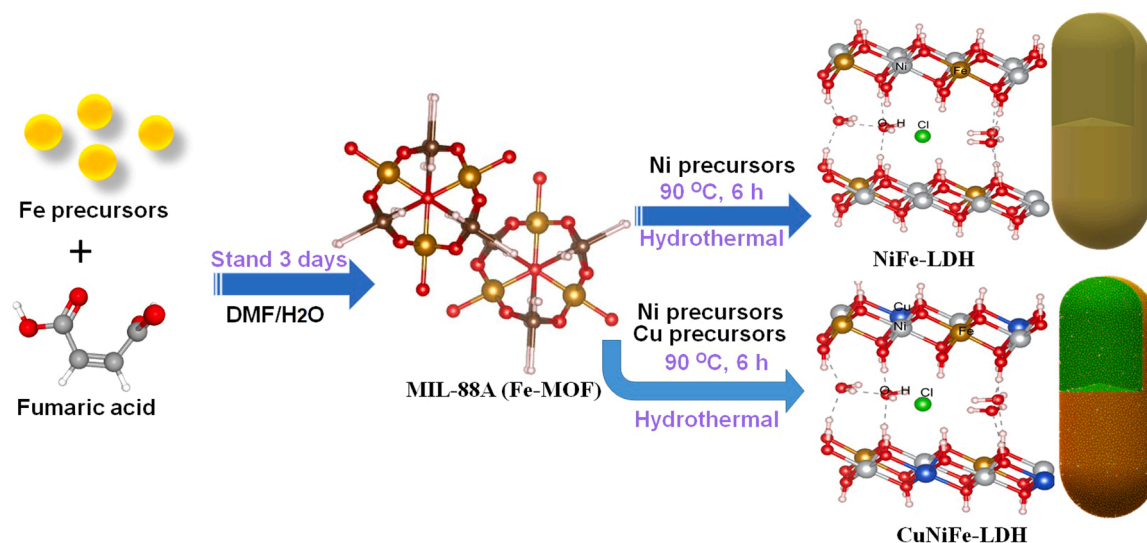
Scheme 1. Schematic illustration of CuNiFe-LDH synthesis process.
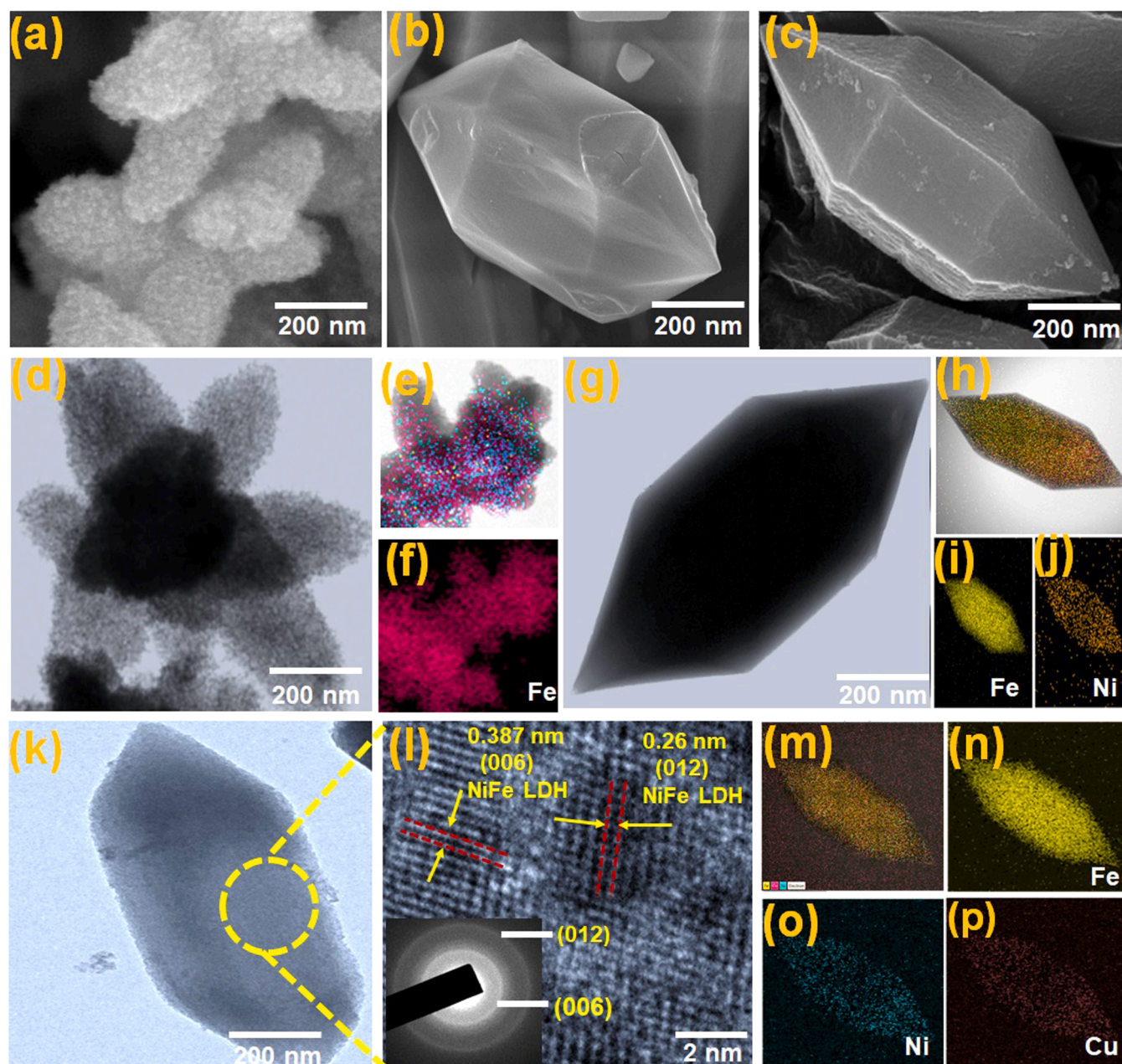
Fig. 1. FESEM images of (a) Fe-MOF, (b) NiFe-LDH nanoprisms, and (c) CuNiFe-LDH nanoprisms; (d–f) TEM image and corresponding EDX elemental mapping images of Fe-MOF, (g–j) TEM image and corresponding EDX elemental mapping images of NiFe-LDH, (k–p) TEM image, HRTEM image with selected area electron diffraction pattern, and corresponding EDX elemental mapping images of CuNiFe-LDH.

3.2. Elemental composition and phase analysis

X-ray photoelectron spectroscopy (XPS) was used to study the electronic structure and composition of CuNiFe-LDH. The survey XPS spectrum of CuNiFe-LDH in Fig. 2a confirms the presence of Ni, Fe, Cu, and O without any impurities. Deconvolution of the Ni 2p spectrum of CuNiFe-LDH (Fig. 2b) reveals two peaks at 856.1 ($2p_{3/2}$) and 873.9 eV ($2p_{1/2}$), which are shifted toward higher binding energies relative to those of NiFe-LDH (Fig. S6) [30,52]. The Fe 2p spectrum of CuNiFe-LDH (Fig. 2c) can be deconvoluted into Fe $2p_{3/2}$ and Fe $2p_{1/2}$ peaks, which are shifted to lower binding energies of 713.6 and 724.4 eV, respectively, relative to those of NiFe-LDH (Fig. S6) [52,53]. The observation of high-intensity Cu peaks at 932.6 eV (Cu $2p_{3/2}$) and 953.3 eV (Cu $2p_{1/2}$) [44,54] confirms the presence of Cu^{2+} species in CuNiFe-LDH (Fig. 2d). The observation of opposite shifts in the Ni 2p and Fe 2p

peaks indicates that partial electron transfer from Ni sites to Fe sites occurs in the presence of Cu in CuNiFe-LDH.

The electron-electron interactions among the Ni, Fe, and Cu ions in CuNiFe-LDH is explained by the electronic structures of the metal ions, as depicted in Fig. 2e. Ni^{2+} has a valence electronic state of d^8 ($t_{2g}^6 e_g^2$), where the fully occupied π-symmetry ᴅ-orbitals (t_{2g}) result in electronic repulsion between Ni^{2+} and O^{2-} [55]. Moreover, Fe^{3+} has unpaired electrons in π-symmetry ᴅ-orbitals (d^5; $t_{2g}^3 e_g^2$), and promote π-back donation and Fe–O bond formation. These interactions can accelerate partial charge transfer from Ni to Fe and lead to the formation of Ni–O–Fe bridges [56]. This behavior is supported by the XPS results. Cu doping facilitates the electron transfer from Ni and Cu to Fe through O atoms in the electron-accepting sites of CuNiFe-LDH. Consequently, a Ni–O–Fe–O–Cu is formed via the ᴅ-orbitals (π-symmetry) of Cu^{2+} ($t_{2g}^6 e_g^3$), resulting in electron–electron repulsion. When coupled with Ni
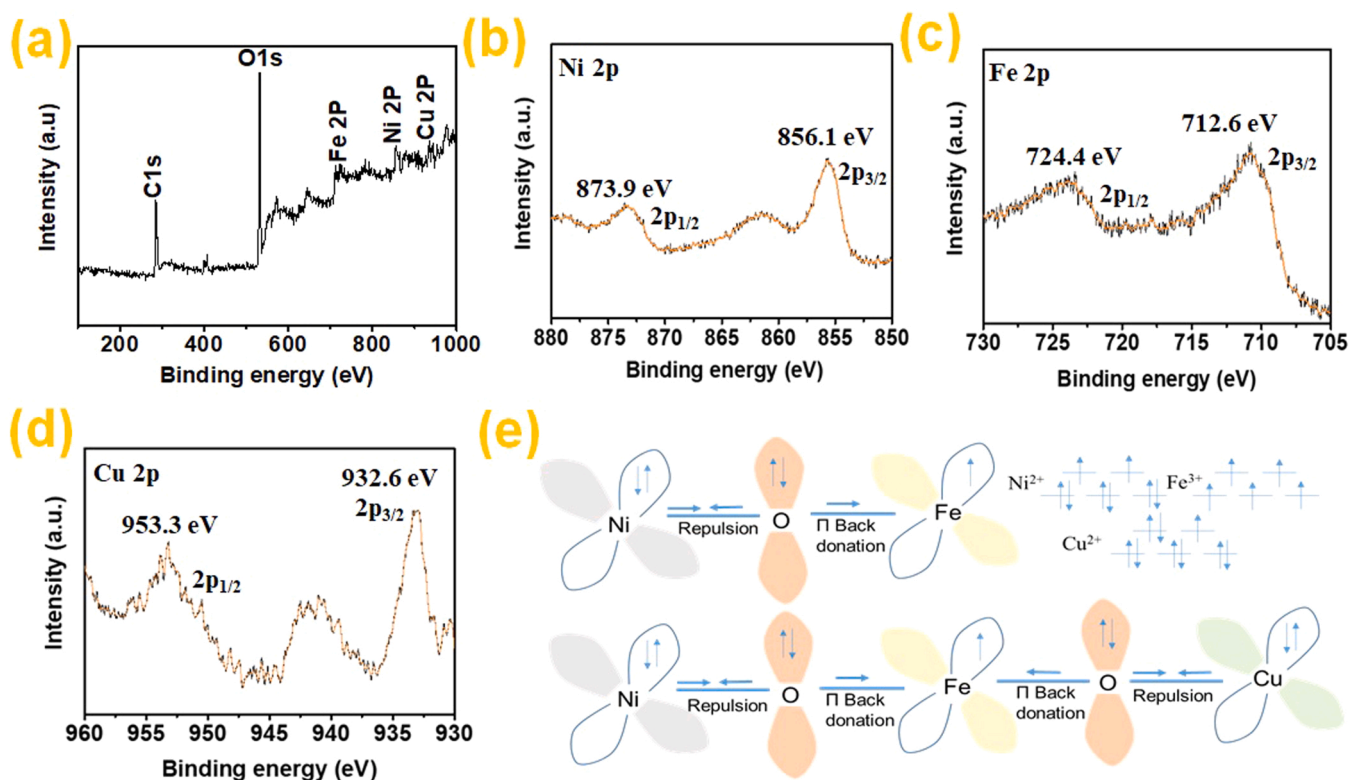
Fig. 2. XPS spectra of CuNiFe-LDH: (a) survey spectra, (b) Ni 2p, (c) Fe 2p, and (d) Cu 2p; (e) schematic illustration of electronic interactions between Ni, Fe, Cu, and O in NiFe-LDH and CuNiFe-LDH.

and Fe, the electron-rich D-orbitals of Cu can modify the e_g electronic state and alter the electronic structure and conductivity of CuNiFe-LDH, leading to improved OER activity.

3.3. Electrochemical measurements
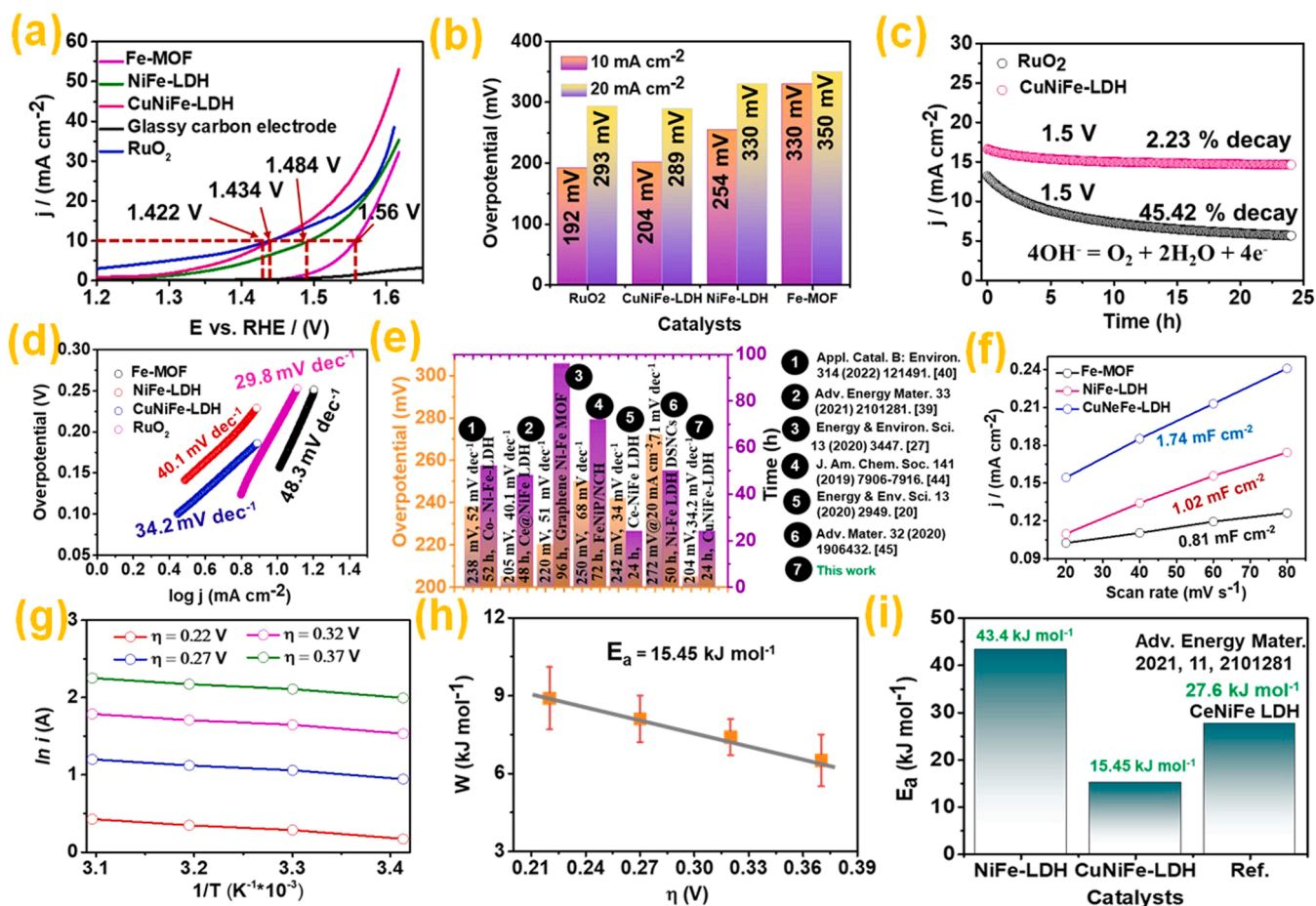
3.3.1. OER activity

To replace RuO_2 and IrO_2, highly efficient OER electrocatalysts are needed. In Fig. S7, experimental results have demonstrated that Cu-NiFe LDH exhibits higher OER activity compared to other first-row transition metals doped in NiFe-LDH. The Brunauer–Emmett–Teller (BET) surface area of CuNiFe-LDH ($\sim$97.5 $m^2 g^{-1}$) is considerably larger than those of Fe-MOF and NiFe-LDH (Fig. S8), and combined physical analyses suggest that the coordination of Cu ions in NiFe-LDH generates larger pore sizes for enhanced electrochemical reactions. Consequently, this catalyst is a promising candidate for electrocatalytic applications. Using a three-electrode arrangement, we compared the OER activity of CuNiFe-LDH, NiFe-LDH, Fe-MOF, and bare glassy carbon (GC) electrodes at the same mass loading (geometrical area: $\sim$200 μg cm^{-2}). As shown in Fig. 3a,b, CuNiFe-LDH exhibits lower η values (204 and 289 mV versus the reversible hydrogen electrode (RHE) at $j = 10$ and 20 mA cm^{-2}, respectively) than NiFe-LDH (254 mV at 10 mA cm^{-2}; 330 mV at 20 mA cm^{-2}), Fe-MOF (330 mV at 10 mA cm^{-2}; 350 at 20 mA cm^{-2}), and bare GC (negligible). Furthermore, the η values of CuNiFe-LDH are similar to those of RuO_2 (192 mV at 10 mA cm^{-2}; 293 mV at 20 mA cm^{-2}) and superior to those of recently published LDH catalysts (Table S3) and MIL-88A MOF-based catalysts (Table S4).

Electrochemical impedance spectroscopy (EIS) was used to estimate the catalyst conductivity and charge transfer resistance (R_{ct}) for the OER process. The Nyquist plots (Fig. S9) fitted using an equivalent circuit (Fig. S10) gave R_{ct} values of 20.4, 5.3, and 1.6 Ω for Fe-MOF, NiFe-LDH, and CuNiFe-LDH, respectively. Thus, the coordination of Cu to NiFe-LDH promotes charge transfer between the active oxygen species and catalytic sites and by optimizing e_g filling, resulting in efficient OER

activity. We also evaluated the catalyst stability using the chronoamperometric method (Ni electrode, catalyst loading: $\sim$185 μg cm^{-2}) at a constant applied V of 1.5 V (Fig. 3c). The CuNiFe-LDH catalyst displays exceptional OER stability during operation over 24 h with a low decay rate of 2.23%, as evidenced by FESEM, FETEM, and EDX analyses (Fig. S11–13). Additionally, ICP-OES analysis (Table S5) showed that the catalysts experienced only minor degradation. In comparison, the RuO_2 electrocatalyst exhibits a much higher decay rate of 45.42%. Furthermore, the Tafel slopes of Fe-MOF, NiFe-LDH, and CuNiFe-LDH are 48.3, 40.1, and 34.2 mV dec^{-1}, respectively (Fig. 3d). The lower Tafel slope of CuNiFe-LDH, which is similar to that of RuO_2 (29.8 mV dec^{-1}), indicates that this catalyst exhibits faster OER reaction kinetics and higher activity. As shown in Fig. 3e, CuNiFe-LDH has a lower η than Co-NiFe-LDH (238 mV),[53] Ce@NiFe-LDH (205 mV),[52] graphene–NiFe-LDH (220 mV),[37] FeNiP/NCH (250 mV) [57], Ce-NiFe-LDH (242 mV),[30] Ni/Ni$_2$P @ N-CNF (285 mV),[18] and NiFe-LDH (272 mV) [58]. The XRD pattern of the CuNiFe LDH catalysts, as shown in Fig. S14, indicates that there is no phase change in the NiFe LDH after the OER stability test. The pattern matches well with the initial XRD pattern, suggesting the structural stability of the catalyst. The high-resolution XPS spectra of Ni 2p, and Fe 2p shown in Fig. S15a-b are almost identical to those of the fresh sample. This similarity implies that there is no change in the composition of Ni and Fe after the OER stability test. However, the high-resolution XPS spectrum of Cu 2p, as depicted in Fig. S15c, shows stronger binding energy peaks after the OER stability test. This confirms the existence of CuO, indicating the oxidation of Cu to CuO [59]. Therefore, we can conclude that the Cu component of the catalyst undergoes oxidation during the OER stability test.

3.3.2. Intrinsic electrocatalytic activity

The intrinsic electrocatalytic activity and OER active sites of the prepared catalysts were evaluated based on the electrochemical active surface area (ECSA) and turnover frequency (TOF). The ECSA of the

Fig. 3. Electrochemical OER activity of Fe-MOF, NiFe-LDH, and CuNiFe-LDH: (a) linear sweep voltammetry curves, (b) overpotentials at 10 and 20 mA cm^{-2}, (c) chronoamperometric stability test of CuNiFe-LDH, (d) Tafel slopes, (e) comparison with recently reported high-performance systems, (f) current densities at different scan rates for electrochemical double-layer capacitance analysis, (g) Arrhenius plots of current at different potentials, (h) activation energy (E_a) calculation, and (i) E_a comparison for NiFe-LDH, CuNiFe-LDH, and CeNiFe-LDH. [52]·Experimental conditions: Ar-saturated 1 M KOH, 20 °C, and catalyst loadings of ~200 and ~185 µg cm^{-2} for GC and Ni electrodes, respectively.

prepared catalysts was investigated by evaluating the electrochemical double-layer capacitance (C_{dl}) at various scan rates in the non-Faradaic region (Fig. S16). By plotting j vs. scan rate (Fig. 3f), we obtained C_{dl} values of 0.8, 1.02, and 1.42 mF cm$_{geo}^{-2}$ for Fe-MOF, NiFe-LDH, and CuNiFe-LDH, respectively. Typically, the average specific capacitance of a flat surface is 40 µF cm^{-2}. The ECSA was calculated from C_{dl} using Equ. 2:

$$\text{ECSA} = C_{dl} \text{ of catalyst (mF cm}^{-2})/0.04 \text{ mF cm}^{-2} \qquad (2)$$

The ECSA of CuNiFe-LDH (35.6 cm$_{ECSA}^{-2}$) is larger than those of NiFe-LDH (25.5 cm$_{ECSA}^{-2}$), and Fe-MOF and (20 cm^{-2} $_{ECSA}$), which can be attributed to the higher electrode/electrolyte interface of this catalyst. The intrinsic electrochemical performance was investigated by normalizing j by the ECSA at a potential of 1.5 V. CuNiFe-LDH exhibits a higher catalytic performance (0.42 mA cm$_{ECSA}^{-2}$) than NiFe-LDH (0.37 mA cm$_{ECSA}^{-2}$) and Fe-MOF (0.10 mA cm$_{ECSA}^{-2}$).

3.3.3. Kinetic energy analysis for the OER

The kinetic energy barrier for the OER was analyzed by calculating the activation energy (E_a) from the LSV curves at different temperatures (Fig. S17). E_a is directly related to the electronic arrangement and composition of electrocatalyst materials. The E_a values were evaluated by plotting the Napierian logarithm of the OER current versus the reciprocal of the absolute temperature in Arrhenius plots ($\frac{\partial(\ln i_0)}{\partial(\frac{1}{T})} = -\frac{E_a}{R}$) (Fig. 3g). The OER current can be expressed as $i_k = A \exp(-\frac{W}{RT})$, where

W is the overall E_a and A is the pre-exponential factor. Finally, the E_a of the OER can be estimated using $W = E_a - \beta\eta$, where β is an experimental constant (Fig. 3h) [60]. As shown in Fig. 3i, the E_a value of CuNiFe-LDH (15.45 kJ mol^{-1}) is lower than those of NiFe-LDH (43.4 kJ mol^{-1}) and CeNiFe-LDH (27.6 kJ mol^{-1}) [52] These findings indicate that CuNiFe-LDH has a lower kinetic barrier for the OER.
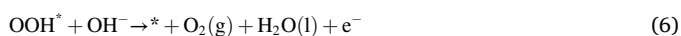
An assessment of the intrinsic activities based on the TOF indicates that CuNiFe-LDH has more efficient catalytic activity for generating O$_2$ molecules. The TOF values were estimated based on the number of Ni, Fe, and Cu sites determined by ICP-OES. CuNiFe-LDH has a much higher TOF value (0.11 s^{-1}) than NiFe-LDH (0.045 s^{-1}) and Fe-MOF (0.024 s^{-1}), which indicates that the coordination of Cu atoms is an effective method to enhance the OER performance of NiFe-LDH.

The superior OER performance of the CuNiFe-LDH catalyst can be explained by several factors. (i) Exposing catalytic sites increases the accessibility to reactants, which can increase the electrocatalytic activity. The assembly of nanoparticles into a porous nanoprism morphology provides more active surface area, thereby improving the transport of electrolyte ions and boosting the catalytic performance. (ii) The catalytic surface with an open network structure is hydrophilic, as indicated by the low contact angle shown in Fig S18. This characteristic allows for enhanced electrolyte permeability. Consequently, this property can facilitate the outgassing of reaction products during electrolysis, thus increasing efficiency. (iii) The tight coupling between Cu and NiFe-LDH facilitates charge and mass transport and promotes charge redistribution at the interface. This synergy can optimize the E_{abs} of reactive

intermediates in catalytic reactions by adjusting the electronic structure. (iv) The hydroxide species generated on the catalyst surface after catalysis provide active sites that are favorable for hydroxyl adsorption, which can accelerate the OER reaction kinetics.

3.4. DFT analysis

DFT calculations were performed to elucidate the underlying OER mechanism and the origin of the enhanced OER performance of CuNiFe-LDH relative to that of NiFe-LDH. We considered the following mechanism for the OER ($4OH^- \rightarrow O_2(g) + 2H_2O(l) + 4e^-$) in an alkaline environment [61,62]·

$$* + OH^- \rightarrow OH^* + e^- \tag{3}$$

$$OH^* + OH^- \rightarrow O^* + H_2O(l) + e^- \tag{4}$$

$$O^* + OH^- \rightarrow OOH^* + e^- \tag{5}$$

$$OOH^* + OH^- \rightarrow * + O_2(g) + H_2O(l) + e^- \tag{6}$$

where * represents an adsorbed state on a catalyst active site. As in previous studies, transition metals with unsaturated coordination at the edge of the LDH catalysts were used as the active sites for the OER [52, 63]. In NiFe-LDH, Ni and Fe atoms can act as active sites for the OER, and the most stable structures of the OER intermediates (OH, O, and OOH) adsorbed on an Fe site are shown in Figs. 4a and S19 as a representative case. The Gibbs free energy differences for the reaction steps were calculated as follows: $\Delta G = \Delta E + \Delta ZPE - T\Delta S$. ΔE was determined using our DFT calculations, and ΔZPE and ΔS were obtained from the literature [64]. The overpotential (η) was calculated as follows:

$$\eta = \max(\Delta G_1, \Delta G_2, \Delta G_3, \Delta G_4)/e - 1.23 V \tag{7}$$

As shown in Fig. 4c, the Fe and Ni sites of NiFe-LDH have different potential-determining steps (PDSs). Eq. (5) ($O^* \rightarrow OOH^*$) is the PDS at the Fe site with an overpotential of 0.98 V. In contrast, the PDS at the Ni site is Eq. (4) ($OH^* \rightarrow O^*$) with an overpotential of 1.65 V. The overpotentials of the two sites indicate that the OER proceeds more readily on Fe sites than on Ni sites in NiFe-LDH.

At an OER potential of 1.6 V, the appearance of two new bands at 477 and 556 cm^{-1} in the Raman spectra (Shown in Fig. S20) indicates the conversion of the LDH into NiOOH, demonstrating that NiOOH is the active phase for the OER. PDSs and overpotentials were also determined for CuNiFe-LDH. At the Cu site, Eq. (3) is the PDS with an overpotential of 0.49 V (Fig. 4b,d). The overpotential at the Cu site in CuNiFe-LDH is lower than that at either the Fe or Ni site in NiFe-LDH, indicating that the Cu site is highly active for the OER. Following Cu doping, the PDSs of the Fe and Ni sites remain Eqs. (5) and (4), respectively. However, interestingly, the overpotentials of the Fe and Ni sites in CuNiFe-LDH (0.58 and 1.36 V, respectively) are lower than those of the Fe and Ni sites in NiFe-LDH (0.98 and 1.65 V, respectively).

Because the activity of the Fe sites is limited by Eq. (5) ($O^* \rightarrow OOH^*$), the difference in adsorption strength between O and OOH is a key factor in determining the overpotential. The adsorption energies of O ($\Delta G(O^*)$) at the Fe site are similar for NiFe-LDH (1.87 eV) and CuNiFe-LDH (1.90 eV). However, the adsorption energy of OOH (($\Delta G(OOH^*)$) decreases from 4.08 eV (NiFe-LDH) to 3.71 eV (CuNiFe-LDH). The weaker OOH adsorption strength at Fe sites caused by Cu doping reduces the overpotential.

In the case of Ni sites with Eq. (4) ($OH^* \rightarrow O^*$) as the PDS, the overpotential is governed by the adsorption strengths of OH and O. Cu doping does not significantly change the adsorption energy of OH ($\Delta G(OH^*)$) at Ni sites (1.05 and 1.09 eV in NiFe-LDH and CuNiFe-LDH, respectively). However, Cu doping decreases the adsorption energy of O from 3.92 to 3.68 eV, leading to CuNiFe-LDH have a lower overpotential than NiFe-LDH. The theoretical volcano plot for the OER overpotential, established using the scaling relation of a wide variety of metal oxide materials in the literature, indicates that $\Delta G(O^*) - \Delta G(OH^*) = \sim 1.6$ eV for an ideal catalyst [65]. As shown in Fig. 4e, the $\Delta G(O^*) - \Delta G(OH^*)$ value of the Cu site in CuNiFe-LDH is within 0.1 eV of the ideal value, which demonstrates that Cu doping of NiFe-LDH provides an excellent OER catalyst.
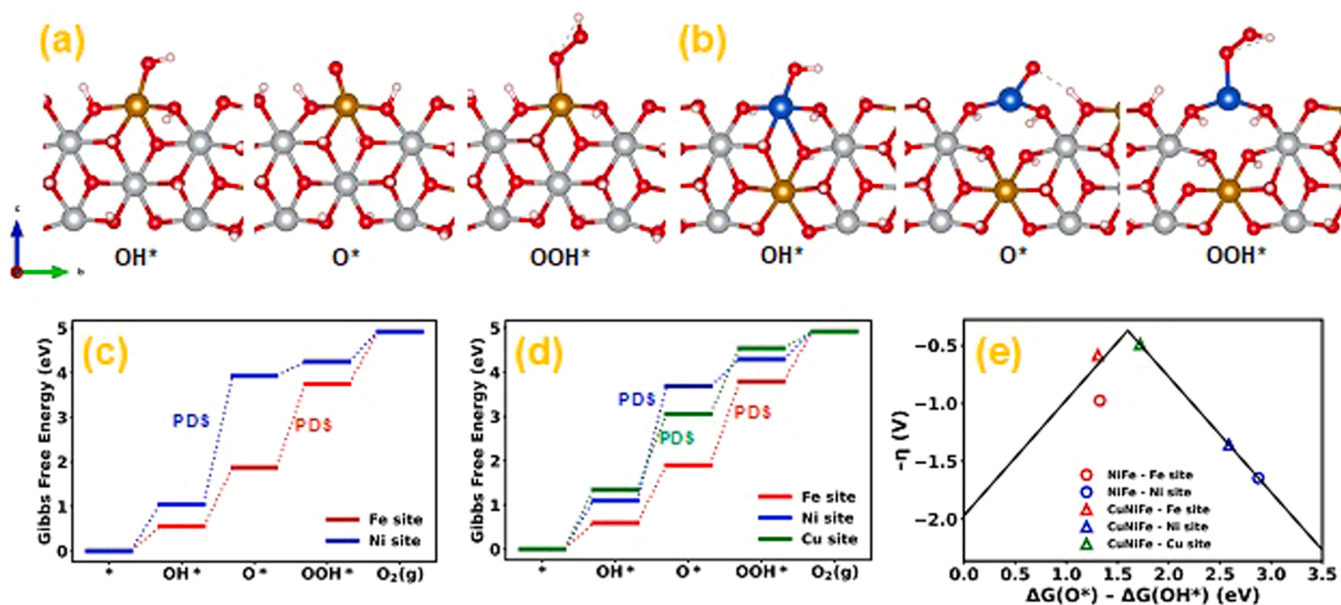

Fig. 4. Optimized structures of OH*, O*, and OOH* on (a) an Fe site in NiFe-LDH and (b) a Cu site in CuNiFe-LDH. The brown, silver, blue, red, and pink spheres represent Fe, Ni, Cu, O, and H atoms, respectively. Free energy diagrams of the OER at zero potential for (c) NiFe-LDH and (d) CuNiFe-LDH. (e) DFT-calculated OER overpotentials (η) as a function of $\Delta G(O^*) - \Delta G(OH^*)$. The black volcano curve was established using the scaling relation $E_{OOH^*} = E_{OH^*} + 3.2 eV$, which has been found to describe a wide variety of metal oxide materials [65].

3.5. Water electrolyzer systems

3.5.1. Conventional two-electrode system

Based on the results in the three-electrode system, CuNiFe-LDH is expected to function as an anode in conventional two-electrode systems. A two-electrode system was developed using CuNiFe-LDH/NFP as the anode and NiFe$_2$O$_4$/NFP [13] or Pt/C/NFP as the cathode. As shown in Fig. 5a, the CuNiFe-LDH/NFP||NiFe$_2$O$_4$/NFP and CuNiFe-LDH/NFP|| Pt/C/NFP systems reach potentials of 1.45 and 1.43 V, respectively, at 10 mA cm^{-2}, comparable to the performance of RuO$_2$/NFP||Pt/C/NFP (1.39 V at 10 mV cm^{-2}), which contains a recognized nonprecious metal catalyst. For the CuNiFe-LDH/NFP||NiFe$_2$O$_4$/NFP and CuNiFe-LDH/NFP||Pt/C/NFP electrode pairs, applied V of 1.72 and 1.682 V, respectively, are required to produce a j value of 50 mA cm^{-2} (Fig. 5b). This activity is similar to that of a Pt/C||RuO$_2$ water splitter, which requires only 1.678 V to reach 50 mA cm^{-2}. Importantly, the j value obtained at 1.85 V for CuNiFe-LDH/NFP||NiFe$_2$O$_4$/NFP is approximately 1.2 times higher than that for RuO$_2$/NFP||Pt/C/NFP.

Overall, the performance trends revealed by the electrolyzer tests with the CuNiFe-LDH/NFP electrode are similar to the results in the three-electrode system (Fig. 3a).

The stability of the CuNiFe-LDH electrode was investigated at j of 10, 25, and 50 mA cm^{-2} (Fig. 5c). A minimal reduction in electrolyzer voltage (0.45%) occurs at $j = 10$ mA cm^{-2}, and further increasing j to 25 and 50 mA cm^{-2} results in insignificant voltage loss (0.85% and 1.57%), respectively. Thus, the stability tests show that the CuNiFe-LDH electrode has excellent stability with negligible activity loss over 90 h. As shown in Fig. 5d and Table S6, the CuNiFe-LDH/NFP(+)||NiFe$_2$O$_4$/NFP (−) and CuNiFe-LDH(+)/NFP||Pt/C/NFP(−) electrode pairs show lower or similar voltages at $j = 10$ mA cm^{-2} with high durability as comparison to recently published high-performance catalysts such as MoS$_2$/ NiFe-LDH(+/−) (1.57 V, 11 h),[66] NiCo$_2$S$_4$@NiFe-LDH(+/−) (1.60 V, 12 h),[67] Cu/Co$_3$Mo(+/−) (1.65 V, 30 h),[68] Fe$_2$O$_3$/NiFe-LDH(+)|| Pt/C(−) (1.47 V, 50 h),[69] Ru/D-NiFe-LDH(+/−) (1.44 V, 100 h),[70] F-CDs/CoP/NF(+/−) (1.50 V, 24 h),[71] CuNWs/NiFe-LDH(+/−) (1.54 V, 48 h)[43] Ni$_{0.8}$Fe$_{0.2}$–AHNA(+)||Ni nanowire array(−) (1.48 V,
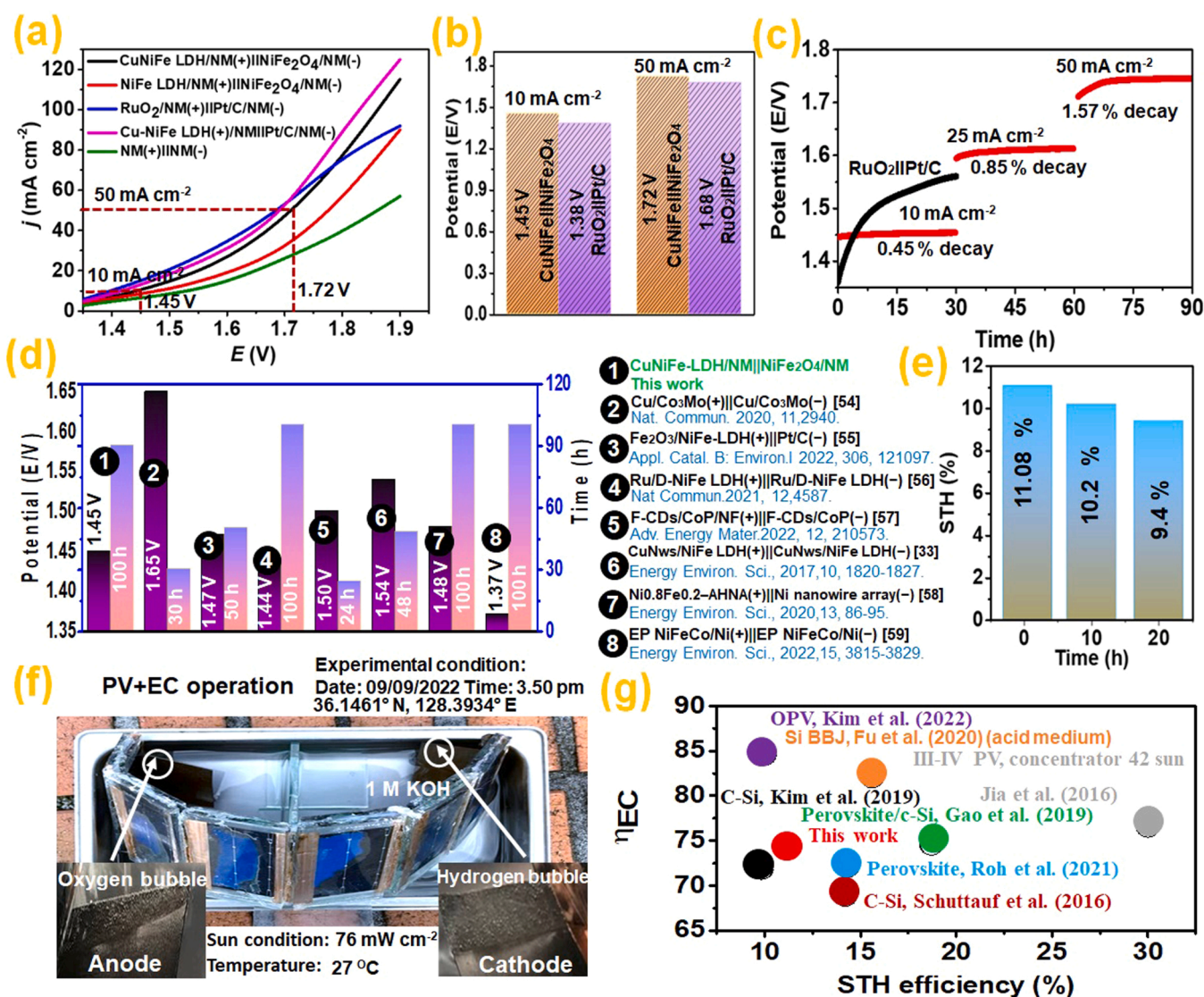
Fig. 5. (a) *I–V* curves for overall water splitting on various electrodes, (b) overall overpotentials of CuNiFe-LDH/ NFP ||NiFe$_2$O$_4$/ NFP and RuO$_2$/ NFP ||Pt/C/ NFP electrode pairs at 10 and 50 mA cm^{-2}, (c) chronopotentiometric stability testing of the CuNiFe-LDH/NFP||NiFe$_2$O$_4$/NFP electrode pair at constant j values of 10, 25, and 50 mA cm^{-2}, (d) comparison of the CuNiFe-LDH/ NFP ||NiFe$_2$O$_4$/ NFP electrode pair with previously reported systems (experimental conditions: Ar-saturated 1 M KOH, 20 °C, ~2.5 mg cm^{-2} catalyst loading, ~0.5 mg cm^{-2} Pt/C loading, and ~1 mg cm^{-2} RuO$_2$ loading), (e) STH efficiency during PV-EC operation, (f) photographs of PV-EC operation (front side, PV side) during actual application in an open environment (experimental conditions: date, 09/09/2022; time, 3:50 pm; geological position, 36.1461° N, 128.3934° E; sun power, 78 W cm^{-2}), and (g) comparison with recently reported PV-EC devices.

100 h),[72] and EP NiFeCo/Ni(+/−) (1.37 V, 100 h) [73].

A digital photograph of the water electrolyzer unit used for hydrogen generation during electrolysis is shown in Fig. S21. By applying a battery source (LR6 AA 1.5 V), vigorous H_2 formation was observed on the cathode surface (**Video S**1). H_2 was captured through a pipe during electrolysis, and the amount of H_2 produced, as determined both experimentally (gas chromatography (GC)) and theoretically, was consistent with the Faradaic efficiency (98.2%; see section S3 in the SI). Additionally, the volumetric ratio of H_2 to O_2 produced was similar to the expected stoichiometric ratio of 1.94:1.06 based on the water-splitting reaction. The observed delay in the appearance of O_2 bubbles may be due to a combination of factors, including the solubility of O_2 in water and the multiple proton-coupled electron transfer steps involved in the OER process.

Supplementary material related to this article can be found online at doi:10.1016/j.apcatb.2023.123187.

3.5.2. Wireless solar-driven water electrolysis

PV-EC water splitting is an efficient tool for producing green H_2. Figs. S22–S26 show images of the PV-EC fabrication process and real devices (flat and semicircular. As shown by the schematic diagram in Figs. S22–26, the PV-EC system includes a c-Si PV module and two electrodes: CuNiFe-LDH/NFP for the OER and $NiFe_2O_4$/NFP [13] for the HER. This configuration ensures that the charge carriers generated in the PV module can flow through the external circuit and participate in electrochemical reactions at the electrodes. The performance of the PV component of the PV-EC device was characterized based on the measured *I–V* curves (Fig. S27). The total solar energy conversion efficiency (PCE) of the PV system in the flat device is 14.9%. As shown in Fig. S27, the short-circuit current (j_{sc} of a PV system refers to the maximum *j* that can flow through the system when it is short-circuited) and open-circuit voltage (V_{oc}) of the device are 9.9 mA cm^{-2} and 2.1 V, respectively. The PV-EC module was designed and independently optimized for the PV and EC components, which can be graphically represented as the intersection of the respective *I–V* curves. As shown in Fig. S28, the intersection provides an operational *j* without bias (j_{op}) of 9.1 mA cm^{-2} at 1.46 V. This value is related to the STH efficiency, as follows:

$$\left[STH = \frac{j_{op} \times (E_{thermo}) \times FE}{P_{IN}} \right]_{AM1.5G} \tag{7}$$

where j_{op} is operational *j* of the device, E_{thermo} (at 25 °C) = 1.23 V, FE is Faradaic efficiency, and P_{IN} is incident light power (1 sun; 1.5 G; 100 mW cm^{-2}). Instead of monitoring *j*, we performed direct gas measurements and used Eq. (7) to calculate the STH efficiency of the device based on the amount of the generated H_2. In the PV-EC device (Fig. 5e), the STH efficiency increases to 11.08% over the first 30 min of operation (stabilization time). This behavior indicates that the energy produced by the PV component (PCE = 14.9%) is converted to H_2 fuel (STH = 11.08%) with an EC conversion efficiency (η_{EC} = STH/PCE) of 74%. Fig. 5e shows STH efficiency over time at room temperature. Over 20 h, the STH efficiency decreases to 9.4%. As this PV-EC device can operate fully for approximately 20 h with a small decrease (17.8%) in STH efficiency, it has good durability for practical applications. Fig. 5f, S29, and S30 show photographs of wireless PV-EC prototype devices (flat and semicircular) in real applications. The epoxy remained stable as long as the penetration of hydroxide ions into the silicon layer was prevented. The decrease in the STH efficiency of the solar cell may be attributable to various factors, including light-induced degradation of the silicon layer (the Staebler–Wronski effect), increased loss due to interfacial coupling, and partial degradation of the catalyst. In practical demonstrations of the planar and semicircular PV-EC systems using a 1.0 M KOH solution, turbulent H_2 and O_2 bubbles were observed (**Video S**2, flat device under solar radiation AM 1.5 G; **Video S**3, semicircular device in open sunlight). Notably, our PV-EC device exhibits better performance than a

recently reported Si-based PV-EC device and other solar-based EC devices (Fig. 5g).

Supplementary material related to this article can be found online at doi:10.1016/j.apcatb.2023.123187.

3.5.3. Commercial AEMWE

We developed a nonprecious-metal-based AEMWE device for low-cost commercial hydrogen production, which can replace PEMWEs (Fig. 6a). The membrane electrode assembly (MEA) was fabricated by combining the CuNiFe-LDH OER electrocatalyst with a previously reported $NiFe_2O_4$ HER electrocatalyst [13] in 1 M KOH using a commercially available anion exchange membrane (Sustainion™ X37–50 RT) as an ionic separator (Fig. S31–32 and **Video S**4 in the SI). The key criteria for improving the MEA as well as the interface between the membrane layer (mL) and catalyst layer (CL) (Figs. S31 and S33) are: (i) High three-phase (solid–liquid–gas) boundaries to create a large reaction zone that facilitates ion and mass transport. (ii) Efficient OH$^-$ transport pathways between the mL and CL. (iii) Good adhesion properties between the CL and mL to avoid catalyst loss during electrolysis. (iv) Use of the anion exchange ionomer binder (Sustainion™ XC-1, Dioxide Materials, USA) to bind the catalyst in the CL, thus preventing catalyst detachment, establish OH$^-$ transport microchannels in the CL.

Supplementary material related to this article can be found online at doi:10.1016/j.apcatb.2023.123187.

A method for direct catalyst deposition on the membrane (CCM) was developed for MEA preparation. The CCM method is suitable for preparing a highly porous CL with ion, gas, and electrolyte permeability. Image of the MEAs prepared using the CCM and CCS (catalyst coated substrate) methods are shown in Fig. S33–34. As shown in Fig. S33, a uniform CL is formed on the membrane surface on the anode (CuNiFe-LDH) and cathode ($NiFe_2O_4$). In the CCS method, CuNiFe-LDH/NFP and $NiFe_2O_4$/NFP electrodes were fabricated as the positive and negative electrodes, respectively (Table S1 in the SI). Fig. 6b shows the load curves of the AEMWE with various MEAs using 1 M KOH as the circulating medium and an operational temperature of 50 °C. The activity of the MEAs in the AEMWE at 1.85 V follow the trend: MEA-CCM-3 (1131 mA cm^{-2}) > MEA-CCS-4 (1080 mA cm^{-2}) > MEA-CCM-1 (1053 mA cm^{-2}) > MEA-CCS-2 (947 mA cm^{-2}). The *j* values of the CuNiFe-LDH/NFP‖$NiFe_2O_4$/NFP(+/−)-CCM-1 and CuNiFe-LDH/NFP‖$NiFe_2O_4$/NFP(+/−)-CCS-2 electrolyzer systems are 1053 and 947 mA cm^{-2}, respectively, at 1.85 V, similar to that of the advanced commercial RuO_2/NFP‖Pt/C/NFP(+/−)-CCS-4 electrode pair (*j* = 1080 mA cm^{-2} at 1.85 V). The highest activity is observed for CuNiFe-LDH/NFP‖Pt/C/NFP(+/−)-CCM-3 (*j* = 1131 mA cm^{-2} at 1.85 V). Thus, our AEMWE device shows excellent performance compared with most recently reported systems (Fig. 6c and Table S7).

Furthermore, EIS measurements were performed to better understand the electrochemical reaction. The Nyquist plot (Fig. S35) of each membrane electrode assembly (MEA), obtained at an applied voltage of 1.85 V, shows a semicircle characteristic. To simulate the EIS data, a basic equivalent electrical circuit was employed. This circuit is depicted as an inset in Fig. S35. In this circuit, R_s (solution and electronic resistance) represents the ohmic resistance of the electrolysis cell, and R_{ct} (R_{kin}, reaction kinetics) represents the charge transfer resistance of the anode. Instead of using capacitance, the constant phase element (CPE) is utilized to characterize the intricate nature of the catalytic layer/electrolyte solution interface, which deviates from being ideally planar [14]. The impedance of the CPE (Z_{CPE}) can be mathematically expressed as follows:

$$Z_{CPE} = A(j_\omega)^{-\alpha}$$

Here, A is equal to $1/C\alpha$, where $C\alpha$ is fixed at a value of 1, representing capacitance that remains unaffected by frequency variations [14]. The parameter α signifies the departure from ideal behavior, with $\alpha = 1$ indicating ideal capacitor characteristics. The symbol ω denotes the
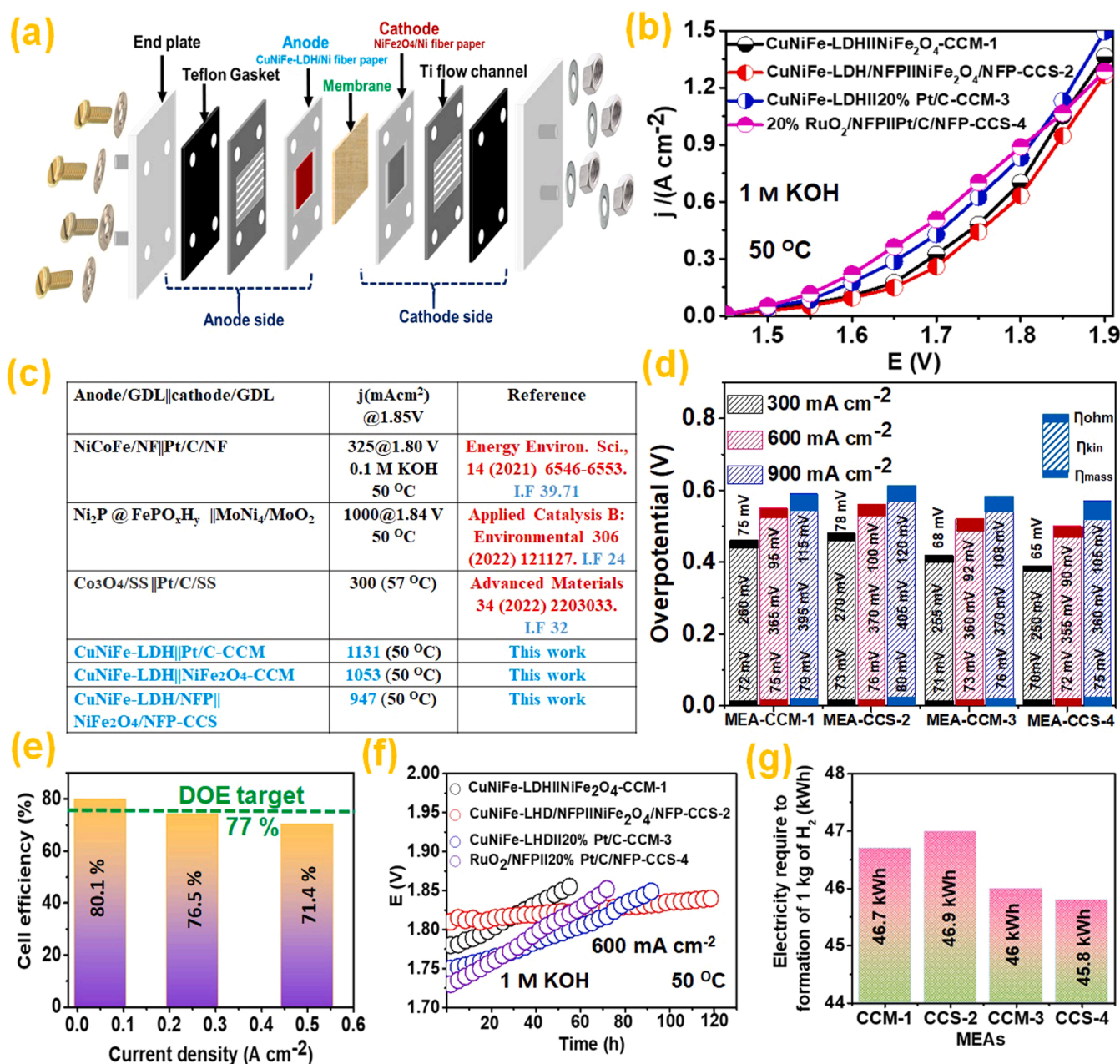
Fig. 6. (a) Schematic illustration of AEMWE operation, (b) polarization curves of AEMWE systems with various MEAs, (c) comparison with previously reported high-performance systems, (d) overall AEMWE overpotential divided into ohmic overpotential (η_{ohm}), kinetic overpotential (η_{kin}), and mass-transfer overpotential (η_{mass}) at low, medium and high j values (300, 600, and 900 mA cm^{-2}, respectively), (e) calculated cell efficiency at various j values, (f) long-term stability of the studied MEAs, and (g) amount of electricity consumed to produce 1 kg of H$_2$ (experimental conditions: 1 M KOH, 50 °C, ~ 2.5 mg cm^{-2} catalyst loading, ~0.5 mg cm^{-2} Pt/C loading, and ~1 mg cm^{-2} RuO$_2$ loading).

angular velocity of the perturbing signal. The ohmic overvoltage (η_{ohm}), kinetic overvoltage (η_{kin}), and mass transport overvoltage (η_{mass}) of each MEA were evaluated at different values of j (300, 600, and 900 mA cm^{-2}) (Fig. 6d and S36). All four MEAs exhibit similar η_{ohm} values, but the η_{kin} and η_{mass} values of the MEAs differ and increase as j increases. Compared with RuO$_2$/NFP||Pt/C/NFP(+/−)-CCS-4, CuNi-Fe-LDH/NFP||Pt/C/NFP(+/−)-CCM-3 has lower η_{kin} and η_{mass} values at $j = 900$ mA cm^{-2}, which indicates that CuNiFe-LDH tends to undergo charge transport processes instead of the OER and that large boundaries between the three phases (solid–liquid–gas) limit the ion diffusion lengths and generate gases [74]. As shown in Fig. 6e, the calculated electrolyzer efficiencies for CCS-2 (E_f) are 80.1%, 76.5%, and 71.4% at j values of 0.05, 0.25, and 0.5 A cm^{-2}, respectively (for details, see

section S4 in the SI), which closely meet the U.S. Department of Energy (DOE) target ($E_f = 77\%$ for water electrolysis).

The durabilities of the MEAs in the AEMWE were evaluated at $j = 600$ mA cm^{-2}. Notably, CuNiFe-LDH/NFP||NiFe$_2$O$_4$/NFP (+/−)-CCS-2 shows excellent stability without significant degradation (0.25 mV h^{-1}) over 120 h (Fig. 6f). The AEMWE system is expected to operate continuously for 600 h upon reaching a voltage of 2 V. The H$_2$ generation rate, as determined by GC, is 20.4 mL min^{-1} with a purity of 99.995%, which is close to commercial quality (99.999%) (Fig. S37). The amount of electricity consumed to form 1 kg of H$_2$ in an industrial alkaline water electrolyzer ($j = 0.5$ A cm^{-2}) was also calculated (for details, see section S5 in the SI). As shown in Fig. 6g, the AEMWE with different MEAs (CCM-1, CCS-2, and CCM-3) requires 46.7, 46.9, and 46

kWh of electricity, respectively, to produce 1 kg of H_2. These values are lower than the target for industrial electrolyzers (48 kWh), suggesting a promising new focus for commercial water electrolysis to achieve sustainable H_2 production.

The overall activity and energy efficiency of the AEMWE can be attributed to several factors: (1) The anion-exchange ionomer binder used in the MEA encapsulates the catalyst nanoparticles, providing more active sites while reducing the ohmic resistance and OH^- transport in the microchannels on the catalyst surface. (2) The unique MEA manufacturing process and uniform pore size enable high gas/liquid mass transfer at the CL/mL interface while allowing efficient bubble transport through the porous NFP layer at a high j value. As evidence, the pore size was measured using Mercury porosimetry, and the average pore diameter was determined to be 22 μm. (3) High three-phase (gas–liquid–solid) boundaries between the CL/mL (as indicated by the X-ray computed tomography (CT) image shown in Fig S38, with calculated triple-phase contact area (%TPCA) is 48.12%, for details, see section S6 in the SI) and ionic binders facilitate charge and mass transport processes while preventing mechanical damage to the catalyst during long-term stability studies. The good adhesion and attachment between the CL and gas diffusion electrode also provide excellent stability.

4. Conclusion

In summary, we introduced a reproducible self-template method for fabricating CuNiFe-LDH nanoprisms with excellent OER activity. The advanced LDH structure of the CuNiFe-LDH microprisms provided an overvoltage of 204 mV at $j = 10$ mA cm^{-2}, a low activation energy ($E_a = 15.45$ kJ mol^{-1}), and high stability over 24 h. The desired nanoprisms were easily produced through Cu-mediated structural modification of the NiFe-LDH structure and MOF modification. DFT calculations demonstrated that the high intrinsic activity of CuNiFe-LDH is attributable to $\Delta G(O^*) - \Delta G(OH^*)$, a key descriptor for predicting the OER performance of the Cu site in CuNiFe-LDH, being close to the ideal value. We coupled the fabricated PV cell with an EC cell composed of CuNiFe-LDH/NFP and NiFe$_2$O$_4$/NFP electrodes to form a PV-EC device, which achieved an STH efficiency of 11.08% with good stability over 20 h. This wireless PV-EC device sets a new benchmark for PV-based solar hydrogen generators. We also used the CuNiFe-LDH catalyst to fabricate AEMWEs with non-noble metal electrodes (anode/cathode) for H_2 production. The obtained devices showed promising efficiency and durability, with a j value of 974 mA cm^{-2} at 1.85 V and stable operation over 120 h. Additionally, only 46.9 kWh of electricity was consumed to form 1 kg of H_2, indicating that this AEMWE could provide a low-cost and sustainable approach for H_2 production.

CRediT authorship contribution statement

Debabrata Chanda: Conceptualization, Investigation, Visualization, Formal analysis, Data curation, Writing − original draft. **Hyunguk Kwon**: Conceptualization, Methodology, Investigation, Writing − original draft. **Jagadis Gautam, Mikiyas Mekete Meshesha, Jang Seok Gwon**: Software, Resources, Methodology. **Minkyu Ju:** Resources, Validation, Methodology, **Kyeounghak Kim**: Conceptualization, Writing − review & editing. **Bee Lyong Yang**: Conceptualization, Supervision, Writing − review & editing, Project administration, Funding acquisition.

Declaration of Competing Interest

The authors declare that they have no known competing financial interests or personal relationships that could have appeared to influence the work reported in this paper.

Data availability

Data will be made available on request.

Acknowledgments

Appendix A. Supporting information

Supplementary data associated with this article can be found in the online version at doi:10.1016/j.apcatb.2023.123187.

References

[1] S. Koumi Ngoh, D. Njomo, An overview of hydrogen gas production from solar energy, Renew. Sustain. Energy Rev. 16 (2012) 6782–6792.

[2] A. Sartbaeva, V.L. Kuznetsov, S.A. Wells, P.P. Edwards, Hydrogen nexus in a sustainable energy future, Energy Environ. Sci. 1 (2008) 79–85.

[3] X. Tian, X. Zhao, Y.-Q. Su, L. Wang, H. Wang, D. Dang, B. Chi, H. Liu, E.J. M. Hensen, X.W. Lou, B.Y. Xia, Engineering bunched Pt-Ni alloy nanocages for efficient oxygen reduction in practical fuel cells, Science 366 (2019) 850–856.

[4] P. Chen, T. Zhou, M. Zhang, Y. Tong, C. Zhong, N. Zhang, L. Zhang, C. Wu, Y. Xie, 3D nitrogen-anion-decorated nickel sulfides for highly efficient overall water splitting, Adv. Mater. 29 (2017), 1701584.

[5] T. Kwon, H. Hwang, Y.J. Sa, J. Park, H. Baik, S.H. Joo, K. Lee, Cobalt assisted synthesis of IrCu hollow octahedral nanocages as highly active electrocatalysts toward oxygen evolution reaction, Adv. Funct. Mater. 27 (2017), 1604688.

[6] J. Su, R. Ge, K. Jiang, Y. Dong, F. Hao, Z. Tian, G. Chen, L. Chen, Assembling Ultrasmall Copper-Doped Ruthenium Oxide Nanocrystals into Hollow Porous Polyhedra: Highly Robust Electrocatalysts for Oxygen Evolution in Acidic Media, Adv. Mater. 30 (2018), 1801351.

[7] N.-T. Suen, S.-F. Hung, Q. Quan, N. Zhang, Y.-J. Xu, H.M. Chen, Electrocatalysis for the oxygen evolution reaction: recent development and future perspectives, Chem. Soc. Rev. 46 (2017) 337–365.

[8] Y. Gorlin, T.F. Jaramillo, A. Bifunctional, Nonprecious metal catalyst for oxygen reduction and water oxidation, J. Am. Chem. Soc. 132 (2010) 13612–13614.

[9] B. Zhang, X. Zheng, O. Voznyy, R. Comin, M. Bajdich, M. García-Melchor, L. Han, J. Xu, M. Liu, L. Zheng, F.P. García de Arquer, C.T. Dinh, F. Fan, M. Yuan, E. Yassitepe, N. Chen, T. Regier, P. Liu, Y. Li, P. De Luna, A. Janmohamed, H.L. Xin, H. Yang, A. Vojvodic, E.H. Sargent, Homogeneously dispersed multimetal oxygen-evolving catalysts, Science 352 (2016) 333–337.

[10] M.A. Mushtaq, M. Arif, X. Fang, G. Yasin, W. Ye, M. Basharat, B. Zhou, S. Yang, S. Ji, D. Yan, Photoelectrochemical reduction of N2 to NH3 under ambient conditions through hierarchical MoSe2@g-C3N4 heterojunctions, J. Mater. Chem. A 9 (2021) 2742–2753.

[11] X.F. Lu, L. Yu, X.W. Lou, Highly crystalline Ni-doped FeP/carbon hollow nanorods as all-pH efficient and durable hydrogen evolving electrocatalysts, Science Advances, 5 eaav6009.

[12] B.R. Wygant, K. Kawashima, C.B. Mullins, Catalyst or precatalyst? The effect of oxidation on transition metal carbide, pnictide, and chalcogenide oxygen evolution catalysts, ACS Energy Lett. 3 (2018) 2956–2966.

[13] D. Chanda, J. Hnát, M. Paidar, J. Schauer, K. Bouzek, Synthesis and characterization of NiFe2O4 electrocatalyst for the hydrogen evolution reaction in alkaline water electrolysis using different polymer binders, J. Power Sources 285 (2015) 217–226.

[14] D. Chanda, J. Hnát, T. Bystron, M. Paidar, K. Bouzek, Optimization of synthesis of the nickel-cobalt oxide based anode electrocatalyst and of the related membrane-electrode assembly for alkaline water electrolysis, J. Power Sources 347 (2017) 247–258.

[15] K. Liu, C. Zhang, Y. Sun, G. Zhang, X. Shen, F. Zou, H. Zhang, Z. Wu, E.C. Wegener, C.J. Taubert, J.T. Miller, Z. Peng, Y. Zhu, High-Performance Transition Metal Phosphide Alloy Catalyst for Oxygen Evolution Reaction, ACS Nano 12 (2018) 158–167.

[16] Y. Li, L. Zhang, X. Xiang, D. Yan, F. Li, Engineering of ZnCo-layered double hydroxide nanowalls toward high-efficiency electrochemical water oxidation, J. Mater. Chem. A 2 (2014) 13250–13258.

[17] Z. Guo, W. Ye, X. Fang, J. Wan, Y. Ye, Y. Dong, D. Cao, D. Yan, Amorphous cobalt–iron hydroxides as high-efficiency oxygen-evolution catalysts based on a facile electrospinning process, Inorg. Chem. Front. 6 (2019) 687–693.

[18] X. Li, J. Zhou, C. Liu, L. Xu, C. Lu, J. Yang, H. Pang, W. Hou, Encapsulation of Janus-structured Ni/Ni2P nanoparticles within hierarchical wrinkled N-doped

carbon nanofibers: Interface engineering induces high-efficiency water oxidation, Appl. Catal. B: Environ. 298 (2021) 120578.

[19] G. Yilmaz, C.F. Tan, M. Hong, G.W. Ho, Functional defective metal-organic coordinated network of mesostructured nanoframes for enhanced electrocatalysis, Adv. Funct. Mater. 28 (2018), 1704177.

[20] H. Yin, Z. Tang, Ultrathin two-dimensional layered metal hydroxides: an emerging platform for advanced catalysis, energy conversion and storage, Chem. Soc. Rev. 45 (2016) 4873–4891.

[21] T. Wang, G. Nam, Y. Jin, X. Wang, P. Ren, M.G. Kim, J. Liang, X. Wen, H. Jang, J. Han, Y. Huang, Q. Li, J. Cho, NiFe (Oxy) Hydroxides Derived from NiFe Disulfides as an Efficient Oxygen Evolution Catalyst for Rechargeable Zn–Air Batteries: The Effect of Surface S Residues, Adv. Mater. 30 (2018), 1800757.

[22] L. Yu, J.F. Yang, B.Y. Guan, Y. Lu, X.W. Lou, Hierarchical Hollow Nanoprisms Based on Ultrathin Ni-Fe Layered Double Hydroxide Nanosheets with Enhanced Electrocatalytic Activity towards Oxygen Evolution, Angew. Chem. Int. Ed. 57 (2018) 172–176.

[23] W. Wang, H. Yan, U. Anand, U. Mirsaidov, Visualizing the conversion of metal–organic framework nanoparticles into hollow layered double hydroxide nanocages, J. Am. Chem. Soc. 143 (2021) 1854–1862.

[24] M.A. Mushtaq, M. Arif, G. Yasin, M. Tabish, A. Kumar, S. Ibraheem, W. Ye, S. Ajmal, J. Zhao, P. Li, J. Liu, A. Saad, X. Fang, X. Cai, S. Ji, D. Yan, Recent developments in heterogeneous electrocatalysts for ambient nitrogen reduction to ammonia: Activity, challenges, and future perspectives, Renew. Sustain. Energy Rev. 176 (2023), 113197.

[25] S. Ibraheem, G. Yasin, A. Kumar, M.A. Mushtaq, S. Ibrahim, R. Iqbal, M. Tabish, S. Ali, A. Saad, Iron-cation-coordinated cobalt-bridged-selenides nanorods for highly efficient photo/electrochemical water splitting, Appl. Catal. B: Environ. 304 (2022), 120987.

[26] R. Gao, J. Zhu, D. Yan, Transition metal-based layered double hydroxides for photo (electro)chemical water splitting: a mini review, Nanoscale 13 (2021) 13593–13603.

[27] X. Li, C. Liu, Z. Fang, L. Xu, C. Lu, W. Hou, Ultrafast room-temperature synthesis of self-supported NiFe-layered double hydroxide as large-current–density oxygen evolution electrocatalyst, Small 18 (2022), 2104354.

[28] L. Ni, J. Zhou, N. Chen, X. Li, S. Xu, L. Zhang, C. Lu, J. Chen, L. Xu, W. Hou, In situ direct growth of flower-like hierarchical architecture of CoNi-layered double hydroxide on Ni foam as an efficient self-supported oxygen evolution electrocatalyst, Int. J. Hydrog. Energy 45 (2020) 22788–22796.

[29] D. Yan, J. Lu, L. Chen, S. Qin, J. Ma, M. Wei, D.G. Evans, X. Duan, A strategy to the ordered assembly of functional small cations with layered double hydroxides for luminescent ultra-thin films, Chem. Commun. 46 (2010) 5912–5914.

[30] H. Xu, C. Shan, X. Wu, M. Sun, B. Huang, Y. Tang, C.-H. Yan, Fabrication of layered double hydroxide microcapsules mediated by cerium doping in metal–organic frameworks for boosting water splitting, Energy Environ. Sci. 13 (2020) 2949–2956.

[31] L. Guo, J. Sun, J. Wei, Y. Liu, L. Hou, C. Yuan, Conductive metal-organic frameworks: Recent advances in electrochemical energy-related applications and perspectives, Carbon Energy 2 (2020) 203–222.

[32] H.-W. Lin, D. Senthil Raja, X.-F. Chuah, C.-T. Hsieh, Y.-A. Chen, S.-Y. Lu, Bi-metallic MOFs possessing hierarchical synergistic effects as high performance electrocatalysts for overall water splitting at high current densities, Appl. Catal. B: Environ. 258 (2019), 118023.

[33] K. Chhetri, T. Kim, D. Acharya, A. Muthurasu, B. Dahal, R.M. Bhattarai, P. C. Lohani, I. Pathak, S. Ji, T.H. Ko, H.Y. Kim, Hollow Carbon Nanofibers with Inside-outside Decoration of Bi-metallic MOF Derived Ni-Fe Phosphides as Electrode Materials for Asymmetric Supercapacitors, Chem. Eng. J. 450 (2022), 138363.

[34] W. Cheng, X. Zhao, H. Su, F. Tang, W. Che, H. Zhang, Q. Liu, Lattice-strained metal–organic-framework arrays for bifunctional oxygen electrocatalysis, Nat. Energy 4 (2019) 115–122.

[35] Z. Chen, B. Fei, M. Hou, X. Yan, M. Chen, H. Qing, R. Wu, Ultrathin Prussian blue analogue nanosheet arrays with open bimetal centers for efficient overall water splitting, Nano Energy 68 (2020) 104371.

[36] W.-D. Zhang, Q.-T. Hu, L.-L. Wang, J. Gao, H.-Y. Zhu, X. Yan, Z.-G. Gu, In-situ generated Ni-MOF/LDH heterostructures with abundant phase interfaces for enhanced oxygen evolution reaction, Appl. Catal. B: Environ. 286 (2021), 119906.

[37] P. Thangavel, M. Ha, S. Kumaraguru, A. Meena, A.N. Singh, A.M. Harzandi, K. S. Kim, Graphene-nanoplatelets-supported NiFe-MOF: high-efficiency and ultra-stable oxygen electrodes for sustained alkaline anion exchange membrane water electrolysis, Energy Environ. Sci. 13 (2020) 3447–3458.

[38] K. Song, S. Liang, X. Zhong, M. Wang, X. Mo, X. Lei, Z. Lin, Tailoring the crystal forms of the Ni-MOF catalysts for enhanced photocatalytic CO_2-to-CO performance, Appl. Catal. B: Environ. 309 (2022), 121232.

[39] J.-X. Feng, H. Xu, Y.-T. Dong, S.-H. Ye, Y.-X. Tong, G.-R. Li, FeOOH/Co/FeOOH Hybrid Nanotube Arrays as High-Performance Electrocatalysts for the Oxygen Evolution Reaction, Angew. Chem. Int. Ed. 55 (2016) 3694–3698.

[40] Z. Chen, T.J. Meyer, Copper(II) Catalysis of Water Oxidation, Angew. Chem. Int. Ed. 52 (2013) 700–703.

[41] M.-T. Zhang, Z. Chen, P. Kang, T.J. Meyer, Electrocatalytic Water Oxidation with a Copper(II) Polypeptide Complex, J. Am. Chem. Soc. 135 (2013) 2048–2051.

[42] X. Cao, E. Johnson, M. Nath, Identifying high-efficiency oxygen evolution electrocatalysts from Co–Ni–Cu based selenides through combinatorial electrodeposition, J. Mater. Chem. A 7 (2019) 9877–9889.

[43] L. Yu, H. Zhou, J. Sun, F. Qin, F. Yu, J. Bao, Y. Yu, S. Chen, Z. Ren, Cu nanowires shelled with NiFe layered double hydroxide nanosheets as bifunctional electrocatalysts for overall water splitting, Energy Environ. Sci. 10 (2017) 1820–1827.

[44] H. Su, S. Song, S. Li, Y. Gao, L. Ge, W. Song, T. Ma, J. Liu, High-valent bimetal Ni_3S_2/Co_3S_4 induced by Cu doping for bifunctional electrocatalytic water splitting, Appl. Catal. B: Environ. 293 (2021), 120225.

[45] Y. Shi, T.-Y. Hsieh, M.A. Hoque, W. Cambarau, S. Narbey, C. Gimbert-Suriñach, E. Palomares, M. Lanza, A. Llobet, High Solar-to-Hydrogen Conversion Efficiency at pH 7 Based on a PV-EC Cell with an Oligomeric Molecular Anode, ACS Appl. Mater. Interfaces 12 (2020) 55856–55864.

[46] M. Lee, B. Turan, J.-P. Becker, K. Welter, B. Klingebiel, E. Neumann, Y.J. Sohn, T. Merdzhanova, T. Kirchartz, F. Finger, U. Rau, S. Haas, A. Bias-Free, Stand-Alone, and Scalable Photovoltaic–Electrochemical Device for Solar Hydrogen Production, Adv. Sustain. Syst. 4 (2020), 2000070.

[47] D. Li, E.J. Park, W. Zhu, Q. Shi, Y. Zhou, H. Tian, Y. Lin, A. Serov, B. Zulevi, E. D. Baca, C. Fujimoto, H.T. Chung, Y.S. Kim, Highly quaternized polystyrene ionomers for high performance anion exchange membrane water electrolysers, Nat. Energy 5 (2020) 378–385.

[48] C.C. Pavel, F. Cecconi, C. Emiliani, S. Santiccioli, A. Scaffidi, S. Catanorchi, M. Comotti, Highly efficient platinum group metal free based membrane-electrode assembly for anion exchange membrane water electrolysis, Angew. Chem. Int. Ed. 53 (2014) 1378–1381.

[49] D. Chanda, J. Hnát, A.S. Dobrota, I.A. Pašti, M. Paidar, K. Bouzek, The effect of surface modification by reduced graphene oxide on the electrocatalytic activity of nickel towards the hydrogen evolution reaction, Phys. Chem. Chem. Phys. 17 (2015) 26864–26874.

[50] D. Li, A.R. Motz, C. Bae, C. Fujimoto, G. Yang, F.-Y. Zhang, K.E. Ayers, Y.S. Kim, Durability of anion exchange membrane water electrolyzers, Energy Environ. Sci. 14 (2021) 3393–3419.

[51] D. Chanda, K. Kannan, J. Gautam, M.M. Meshesha, S.G. Jang, V.A. Dinh, B.L. Yang, Effect of the interfacial electronic coupling of nickel-iron sulfide nanosheets with layer Ti_3C_2 MXenes as efficient bifunctional electrocatalysts for anion-exchange membrane water electrolysis, Appl. Catal. B: Environ. 321 (2023), 122039.

[52] M. Liu, K.-A. Min, B. Han, L.Y.S. Lee, Interfacing or Doping? Role of Ce in Highly Promoted Water Oxidation of NiFe-Layered Double Hydroxide, Adv. Energy Mater. 11 (2021) 2101281.

[53] Y. Yang, S. Wei, Y. Li, D. Guo, H. Liu, L. Liu, Effect of cobalt doping-regulated crystallinity in nickel-iron layered double hydroxide catalyzing oxygen evolution, Appl. Catal. B: Environ. 314 (2022), 121491.

[54] Y. Ma, K. Wang, D. Liu, X. Yang, H. Wu, C. Xiao, S. Ding, Surface dual-oxidation induced metallic copper doping into NiFe electrodes for electrocatalytic water oxidation, J. Mater. Chem. A 7 (2019) 22889–22897.

[55] S. Zhao, Y. Wang, J. Dong, C.-T. He, H. Yin, P. An, K. Zhao, X. Zhang, C. Gao, L. Zhang, J. Lv, J. Wang, J. Zhang, A.M. Khattak, N.A. Khan, Z. Wei, J. Zhang, S. Liu, H. Zhao, Z. Tang, Ultrathin metal–organic framework nanosheets for electrocatalytic oxygen evolution, Nat. Energy 1 (2016) 16184.

[56] J. Jiang, F. Sun, S. Zhou, W. Hu, H. Zhang, J. Dong, Z. Jiang, J. Zhao, J. Li, W. Yan, M. Wang, Atomic-level insight into super-efficient electrocatalytic oxygen evolution on iron and vanadium co-doped nickel (oxy)hydroxide, Nat. Commun. 9 (2018) 2885.

[57] Y.-S. Wei, M. Zhang, M. Kitta, Z. Liu, S. Horike, Q. Xu, A Single-Crystal, Open-Capsule Metal–Organic Framework, J. Am. Chem. Soc. 141 (2019) 7906–7916.

[58] J. Zhang, L. Yu, Y. Chen, X.F. Lu, S. Gao, X.W. Lou, Designed Formation of Double-Shelled Ni–Fe Layered-Double-Hydroxide Nanocages for Efficient Oxygen Evolution Reaction, Adv. Mater. 32 (2020), 1906432.

[59] L. Yu, G. Li, X. Zhang, X. Ba, G. Shi, Y. Li, P.K. Wong, J.C. Yu, Y. Yu, Enhanced Activity and Stability of Carbon-Decorated Cuprous Oxide Mesoporous Nanorods for CO_2 Reduction in Artificial Photosynthesis, ACS Catal. 6 (2016) 6444–6454.

[60] H. Han, K.M. Kim, J.H. Ryu, H.J. Lee, J. Woo, G. Ali, K.Y. Chung, T. Kim, S. Kang, S. Choi, J. Kwon, Y.-C. Chung, S. Mhin, T. Song, Boosting oxygen evolution reaction of transition metal layered double hydroxide by metalloid incorporation, Nano Energy 75 (2020) 104945.

[61] M. García-Mota, M. Bajdich, V. Viswanathan, A. Vojvodic, A.T. Bell, J.K. Nørskov, Importance of Correlation in Determining Electrocatalytic Oxygen Evolution Activity on Cobalt Oxides, J. Phys. Chem. C 116 (2012) 21077–21082.

[62] N.H. Kwon, M. Kim, X. Jin, J. Lim, I.Y. Kim, N.-S. Lee, H. Kim, S.-J. Hwang, A rational method to kinetically control the rate-determining step to explore efficient electrocatalysts for the oxygen evolution reaction, NPG Asia Mater. 10 (2018) 659–669.

[63] P. Li, X. Duan, Y. Kuang, Y. Li, G. Zhang, W. Liu, X. Sun, Tuning Electronic Structure of NiFe Layered Double Hydroxides with Vanadium Doping toward High Efficient Electrocatalytic Water Oxidation, Adv. Energy Mater. 8 (2018), 1703341.

[64] P. Liao, J.A. Keith, E.A. Carter, Water Oxidation on Pure and Doped Hematite (0001) Surfaces: Prediction of Co and Ni as Effective Dopants for Electrocatalysis, J. Am. Chem. Soc. 134 (2012) 13296–13309.

[65] I.C. Man, H.-Y. Su, F. Calle-Vallejo, H.A. Hansen, J.I. Martínez, N.G. Inoglu, J. Kitchin, T.F. Jaramillo, J.K. Nørskov, J. Rossmeisl, Universality in Oxygen Evolution Electrocatalysis on Oxide Surfaces, ChemCatChem 3 (2011) 1159–1165.

[66] P. Xiong, X. Zhang, H. Wan, S. Wang, Y. Zhao, J. Zhang, D. Zhou, W. Gao, R. Ma, T. Sasaki, G. Wang, Interface modulation of two-dimensional superlattices for efficient overall water splitting, Nano Lett. 19 (2019) 4518–4526.

[67] J. Liu, J. Wang, B. Zhang, Y. Ruan, L. Lv, X. Ji, K. Xu, L. Miao, J. Jiang, Hierarchical $NiCo_2S_4$@NiFe LDH heterostructures supported on nickel foam for enhanced overall-water-splitting activity, ACS Appl. Mater. Interfaces 9 (2017) 15364–15372.

[68] H. Shi, Y.-T. Zhou, R.-Q. Yao, W.-B. Wan, X. Ge, W. Zhang, Z. Wen, X.-Y. Lang, W.-T. Zheng, Q. Jiang, Spontaneously separated intermetallic Co_3Mo from nanoporous

copper as versatile electrocatalysts for highly efficient water splitting, Nat. Commun. 11 (2020) 2940.

[69] C.-F. Li, L.-J. Xie, J.-W. Zhao, L.-F. Gu, J.-Q. Wu, G.-R. Li, Interfacial electronic modulation by Fe2O3/NiFe-LDHs heterostructures for efficient oxygen evolution at high current density, Appl. Catal. B: Environ. 306 (2022), 121097.

[70] P. Zhai, M. Xia, Y. Wu, G. Zhang, J. Gao, B. Zhang, S. Cao, Y. Zhang, Z. Li, Z. Fan, C. Wang, X. Zhang, J.T. Miller, L. Sun, J. Hou, Engineering single-atomic ruthenium catalytic sites on defective nickel-iron layered double hydroxide for overall water splitting, Nat. Commun. 12 (2021) 4587.

[71] H. Song, J. Yu, Z. Tang, B. Yang, S. Lu, Halogen-doped carbon dots on amorphous cobalt phosphide as robust electrocatalysts for overall water splitting, Adv. Energy Mater. 12 (2022), 2102573.

[72] C. Liang, P. Zou, A. Nairan, Y. Zhang, J. Liu, K. Liu, S. Hu, F. Kang, H.J. Fan, C. Yang, Exceptional performance of hierarchical Ni–Fe oxyhydroxide@NiFe alloy nanowire array electrocatalysts for large current density water splitting, Energy Environ. Sci. 13 (2020) 86–95.

[73] J. Mo, Y. Ko, Y.S. Yun, J. Huh, J. Cho, A carbonization/interfacial assembly-driven electroplating approach for water-splitting textile electrodes with remarkably low overpotentials and high operational stability, Energy Environ. Sci. 15 (2022) 3815–3829.

[74] L. Wan, Z. Xu, Q. Xu, P. Wang, B. Wang, Overall design of novel 3D-ordered MEA with drastically enhanced mass transport for alkaline electrolyzers, Energy Environ. Sci. 15 (2022) 1882–1892.